# Bilateral Filtering of Diffusion Tensor Magnetic Resonance Images

Ghassan Hamarneh and Judith Hradsky

*Abstract*—We extend the well-known scalar image bilateral filtering technique to diffusion tensor magnetic resonance images (DTMRI). The scalar version of bilateral image filtering is extended to perform edge-preserving smoothing of DT field data. The bilateral DT filtering is performed in the Log-Euclidean framework which guarantees valid output tensors. Smoothing is achieved by weighted averaging of neighboring tensors. Analogous to bilateral filtering of scalar images, the weights are chosen to be inversely proportional to two distance measures: The geometrical Euclidean distance between the spatial locations of tensors and the dissimilarity of tensors. We describe the noniterative DT smoothing equation in closed form and show how interpolation of DT data is treated as a special case of bilateral filtering where only spatial distance is used. We evaluate different recent DT tensor dissimilarity metrics including the Log-Euclidean, the similarity-invariant Log-Euclidean, the square root of the J-divergence, and the distance scaled mutual diffusion coefficient. We present qualitative and quantitative smoothing and interpolation results and show their effect on segmentation, for both synthetic DT field data, as well as real cardiac and brain DTMRI data.

*Index Terms*—Bilateral filtering, diffusion tensor magnetic resonance imaging (DTMRI), interpolation, smoothing.

## I. INTRODUCTION

**D**IFFUSION is the process by which molecules are transported from one part of a medium to another. The flux of diffusing molecules is a result of their random Brownian motion in concentration gradients and is described by Fick's law. Diffusion tensor magnetic resonance imaging (DTMRI) records the diffusion characteristics of water molecules along fiber tracts *in vivo* and is becoming increasingly valuable for assessing the effects of disease progression and treatment evaluation on fiber connectivity and diffusion properties [1]–[3]. In DTMRI, typically each voxel of the 3-D image is assigned a rank three, second order diffusion tensor forming a 3-D tensor field. Each tensor is expressed as a $3 \times 3$ symmetric, positive semi-definite (PSD) matrix (with nonnegative eigenvalues). Each tensor is the covariance matrix of a tri-variate Gaussian probability density function of water molecule displacement (in $x$, $y$, and $z$ directions) at each lattice point in the image.

The general classes of medical image processing and analysis algorithms performed on scalar medical images (e.g., filtering, segmentation, registration and visualization of X-ray CT, T1-weighted MRI, ultrasound, and others) need to be extended to DTMRI tensor fields in order to glean quantitative and qualitative information, potentially improving computer aided diagnosis, follow up of treatment and disease progression, and statistical analysis of structural and functional variability. In the following paragraphs we review important contributions in processing, segmentation, registration, and visualization of tensor field data.

The primary goal of processing is to reduce the noise in the DTMRI data that occurs due to various imaging acquisition artifacts. There exist numerous techniques for image processing of scalar fields; an essential task in any image processing pipeline. However, only a few methods have been recently extended to perform basic processing and reduce noise in diffusion tensor image data; for example median filtering, morphological operations, interpolation, and anisotropic edge preserving smoothing [4]–[8].

Identifying and delineating regions of interest (ROI) in image data is necessary for performing subsequent quantitative analysis and qualitative visualization. Segmentation methods typically rely on a) identifying nearby voxels with similar diffusion properties and grouping them into one coherent structure, b) identifying edges in the DTMRI and linking them to form separating boundaries between neighboring structures, and c) incorporating prior knowledge about the shape characteristics of the different target structures to segment. These intuitive ideas are very well understood for the scalar case, but have only recently been the focus of research for tensor fields [9]–[20].

To facilitate viewing and interrogating DTMRI segmentation and visualization results within the context of other medical imaging modalities (e.g., structural MRI), the data sets must be properly fused by bringing them into proper spatial alignment. Image registration is also needed for quantitative and qualitative longitudinal analysis tasks in which DTMRI data of the same subject at different times must be compared [21]–[24].

Given the tensor field data structure many standard visualization techniques can not be directly applied [3], [25]. A simple approach is to first calculate scalar quantities from the tensor fields, for example apparent diffusion coefficient (ADC), relative anisotropy (RA), fractional anisotropy (FA), and volume ratio, and then use available visualization software implementing standard algorithms, including multiplanar reconstruction using orthographic and oblique slices, volume rendering using ray casting or maximum intensity projection, and iso-surface rendering. Although this approach is simple

it is generally not recommended, as most of the information in the tensors will be lost. As DTs can be described by three eigenvectors and three strictly positive eigenvalues, an alternative straightforward way of visualizing DT fields is via 3-D ellipsoids whose orientations are given by the eigenvectors and the length of their semi-axes by the eigenvalues. Given some visual ambiguities of the ellipsoidal representation, an extended superquadrics approach was proposed [26]. Although very insightful, these glyph-type approaches are not sufficient to accomplish the important goal of visualizing fiber tracts; therefore, advanced tractography visualization tools such as stream tubes were developed [27], [28].

It is also worthwhile mentioning that different software tools are being developed to perform some of the tasks mentioned above (such as BioTensor [29], DoDTI [30], and others [31]–[36]). However, there remains a substantial amount of research to be performed to develop libraries for DT processing, segmentation, registration, and visualization, at par with what is available for scalar images.

None of the previously proposed methods or available software provides an algorithm for performing bilateral filtering on DTMRI data. In this paper,[1] we extend the well-known scalar image bilateral filtering technique to DTMRI. We propose a bilateral diffusion tensor filtering algorithm, which carries the same intuitive ideas as of its scalar field counterpart: similar and proximate data are given higher weights. Towards this goal, diffusion tensors must be averaged appropriately without producing invalid tensors, and similarity between tensor values must be calculated in a meaningful way. In order to realize this extension, we make use of two major recent advancements in the field of DTMRI processing, namely the Log-Euclidean framework for diffusion tensor calculus and diffusion tensor dissimilarity measures. We further show how DT interpolation is treated as a special case of bilateral filtering where only spatial distance is used.

We evaluate different alternative DT dissimilarity metrics including the Log-Euclidean, the similarity-invariant Log-Euclidean, the square root of the J-divergence, and the distance scaled mutual diffusion coefficient [38], [10], [39]. The closest published work to ours is that of Westin and Knutson [8]. The filtering they proposed uses normalized convolution and does not use tensor dissimilarity metrics. Further, they do not weight neighbors based on geometric and tensor distance. This previous work also lacks qualitative results.

The remainder of the paper is organized as follows. Following a brief review of bilateral filtering for scalar images in Section II-A, we motivate the need for a special treatment for DTMRI data. We then propose the closed form solution for bilateral filtering of DT fields and describe its reliance on the Log-Euclidean framework and the tensor dissimilarity measures (Sections II-B and II-C). In Section III, we first briefly describe the clinical context of our work, then present qualitative and quantitative smoothing and interpolation on synthetic as well as real (cardiac and brain) DTMRI images. We demonstrate the performance of the proposed methods with different choices of free parameters as well as alternative

tensor dissimilarity measures. We also present the effect of bilateral DT filtering on an extension of "livewire" to DTMRI. We summarize and draw conclusions in Section IV.

## II. BILATERAL FILTERING OF DTMRI

### A. Bilateral Filtering of Scalar Images

Bilateral filtering smoothes image data while preserving edges by means of a weighted averaging of nearby image values [40]. For an input image $f(x)$, the filtered output image $h(x)$ is defined as follows:

$$h(x) = k(x)^{-1} \int_{-\infty}^{\infty} \int_{-\infty}^{\infty} f(\xi) c(\xi, x) s(f(\xi), f(x)) d\xi$$

(1)

$$k(x) = \int_{-\infty}^{\infty} \int_{-\infty}^{\infty} c(\xi, x) s(f(\xi), f(x)) d\xi$$

(2)

where $c(\xi, x)$ is inversely proportional to the spatial distance between the neighborhood center $x$ and a nearby location $\xi$, and $s(f(\xi), f(x))$ is proportional to the photometric similarity (e.g., in grey level values) between the image function at $x$ and $\xi$. This essentially means that image values with closer spatial and photometric proximity contribute more to the output filtered pixel, by having a higher weight in a weighted-average implementation.[2]

For DTMRI data, calculating the spatial proximity (Euclidean distance) of tensors in the image domain clearly remains the same as in the scalar case. However, as described above, bilateral filtering also relies on calculating a measure of similarity between the data values at neighboring pixels. For scalar images, the difference between the intensity of two pixels can be simply obtained as the absolute difference (using simple subtraction). However, since for DTMRI the values at pixels are DTs (PSD matrices, not scalars), an appropriate dissimilarity metric between DTs must be calculated. Such metrics must simultaneously consider the difference in the magnitudes and directions of the diffusion and, therefore, respect the non-Euclidean space of DTs. Calculating the difference as the Euclidean distance, in 9-D space ($3 \times 3$ DT matrix) or 6-D (given the matrix symmetry), of the original tensor entries, makes the implicit assumption that the hyper-line connecting such two tensors in 9-D (or 6-D) is a valid space of tensors, which is incorrect. Similar argument can be made for averaging tensors. For example, linear averaging of each DT component separately suffers from a "swelling effect," where DTs with the same determinant will result in an average with a larger determinant [42]. Although averaging each component of eigenvalues independently will result in PSD matrices (weighted averaging of nonnegative eigenvalues remains nonnegative), however, one cannot ignore the directions of the eigen vectors. For example, averaging two tensors, with identical eigenvalues and different eigenvector orientations, via averaging only their eigen values will result in a new tensor with exactly the same eigenvalues

[1]This work is based on a previous conference presentations [37].

[2]Trilateral filtering has been recently proposed to take texture of scalar intensity images into account as well [41].

but without any dependence on the original directions of the eigenvectors of the original tensors.

In order to take the whole tensor into account, a proper tensor dissimilarity metric must be used which simultaneously takes into account all the six degrees of freedom in the DT using appropriate metrics intrinsic to the space of PSD matrices. Therefore, two important operations must be redefined for tensor fields, namely, weighted-averaging of DTs and calculating tensor dissimilarity.

### B. Weighted Averaging of Diffusion Tensors

Diffusion tensors do not form a vector space since they are symmetric PSD matrices whose space is restricted to a convex half-cone [43]. Therefore, special care needs to be taken when performing calculations and statistics on diffusion tensors. For example, simply subtracting two DTs in general gives an invalid DT [44], [43]. Arsigny *et al.* recently proposed the Log-Euclidean Riemannian framework allowing simple tensor computations in the domain of matrix logarithms [38]. Specifically, for our proposed extension of bilateral smoothing to tensor fields, we adopt the Log-Euclidean framework and define the weighted average of tensors as

$$T(x) = \text{expm}\left(\sum_{i=1}^{N}(w_i(x)/k(x))\text{logm}(T(\xi_i))\right) \quad (3)$$

$$k(x) = \sum_{i=1}^{N} w_i(x) \quad (4)$$

where $T(x)$ is the tensor resulting from Log-Euclidean, weighted averaging of $N$ tensors, $T(\xi_i)$, in the neighborhood of $x$, with corresponding weights $w_i(x)$. expm and logm denote matrix exponential and logarithm, respectively. To perform DT smoothing, (3) replaces each tensor at every location $x$ in the image by a weighted average of $N$ neighboring tensors $T(\xi_i)$. For example, $N = 9$ for a $3 \times 3$ 8-connected 2-D neighborhood, and $N = 27$, for a $3 \times 3 \times 3$ 26-connected 3-D neighborhood.

The smoothing effect now clearly depends on the choice of the weights, $w_i(x)$. A simple implementation of (equalweight) averaging is achieved by setting $w_i(x) = 1/N, \forall i$. However, this operation blurs interfaces between tissues of different diffusion properties; e.g., white and gray matter in the brain. This is where the bilateral filtering ideas are essential for edge-preserving smoothing. Towards this end, to replace the tensor at each pixel in the image, we define the weights to be inversely proportional to the spatial distance and the tensor dissimilarity between the neighboring tensors and the center tensor, according to

$$w_i(x) = \alpha f_1(d_T(T(x), T(\xi_i))) + (1 - \alpha)f_2(d_S(x, \xi_i)) \quad (5)$$

where $d_T(T(x), T(\xi_i))$ is the tensor dissimilarity between $T(x)$ and $T(\xi_i)$, $d_S(x, \xi_i)$ is the spatial Euclidean distance between $x$ and $\xi_i$. $f_1$ and $f_2$ are monotonically decreasing functions that map the range of tensor-dissimilarity values and spatial distances, respectively, to the interval [0,1], yielding measures of tensor similarity and spatial proximity, respectively. We used $f_i(z) = (z - z_{\max})/(z_{\min} - z_{\max})$ for linear mapping and

$f_i(z) = \log(z_{\max} - z + 1)/(\log(z_{\max} - z_{\min} + 1))$ for logarithmic mapping). $\alpha \in [0, 1]$ controls the relative emphasis on spatial versus tensor distance.

### C. Diffusion Tensor Dissimilarity

What remains is a proper definition of tensor dissimilarity, $d_T(T_1, T_2)$, between two tensors, $T_1$ and $T_2$. The Frobenius norm, for example, $\|T_1 - T_2\|_F$, where $\|A\|_F = \sqrt{\text{trace}(AA^H)}$, would be a possible choice had the diffusion tensors spanned a Euclidean space. However, given the PSD nature of the diffusion tensors, such measure of dissimilarity is inappropriate, as discussed and motivated earlier (Section II-A).

We compare four recently proposed approaches for calculating tensor dissimilarity: The Log-Euclidean distance, the similarity-invariant Log-Euclidean distance [38], the affine-invariant square root of the J-divergence [10], and the distance scaled mutual diffusion coefficient [39], denoted respectively as $d_{T_{1,F}}, d_{T_{1,FI}}, d_{T_J}, d_{T_K}$, and are given by

$$d_{T_{1,F}}(T_1, T_2) = \|\text{logm}(T_1) - \text{logm}(T_2)\|_F \quad (6)$$

$$d_{T_{1,FI}}(T_1, T_2) = \sqrt{\text{trace}((\text{logm}(T_1) - \text{logm}(T_2))^2)} \quad (7)$$

$$d_{T_J}(T_1, T_2) = \frac{1}{2}\sqrt{\text{trace}(T_1^{-1}T_2 + T_2^{-1}T_1) - 2n} \quad (8)$$

$$d_{T_K}(T_1, T_2) = \frac{[(v'T_1v)(v'T_2v)]^\gamma}{\sigma^2} \quad (9)$$

$$v = (x_1 - x_2)/\sigma, \sigma = \|x_1 - x_2\|, \gamma = 1$$

where $\|\cdot\|$ denotes the $L_2$-vector norm ($|\cdot|_2$), $x_i$ describes the location of $T_i$ (see [39] for details), and $n$ is the size of the square tensor, i.e., $n = 3$ for 3-D diffusion.

### D. Bilateral DTMRI Filtering and Interpolation

Applying (3) at each voxel in the DTMRI volume, with weights as in (5) and with tensor distance as in (6)–(9), results in a closed-form, edge-preserving filtering extending the original scalar bilateral filter to diffusion tensor data. The proposed method is noniterative. Nevertheless, multiple smoothing iterations can still be performed as is typical in scalar image filtering algorithms. Further, we handle diffusion tensor field interpolation as a special case of bilateral filtering (3) as follows. We interpolate a tensor at any nongrid position as the Log-Euclidean weighted sum of $N$ nearby tensors, $T(\xi)$, where the weights are inversely proportional to *only* the spatial distance between the nongrid position $x$ and the locations, $\xi$, of the nearby tensors. This is intuitively and conveniently obtained by setting $\alpha = 0$ in (5).

## III. EXPERIMENTS AND RESULTS

The proposed DT bilateral filtering is used for preprocessing of DTMRI data related to two long term clinical applications. First, we are investigating the disease progression and treatment in multiple sclerosis patients on interhemispheric fiber connectivity and diffusion properties within different regions of the callosum (CC) bridge [45], [46]. Second, we are studying the properties of the laminar cardiac fiber sheet in the myocardium from DTMRI.
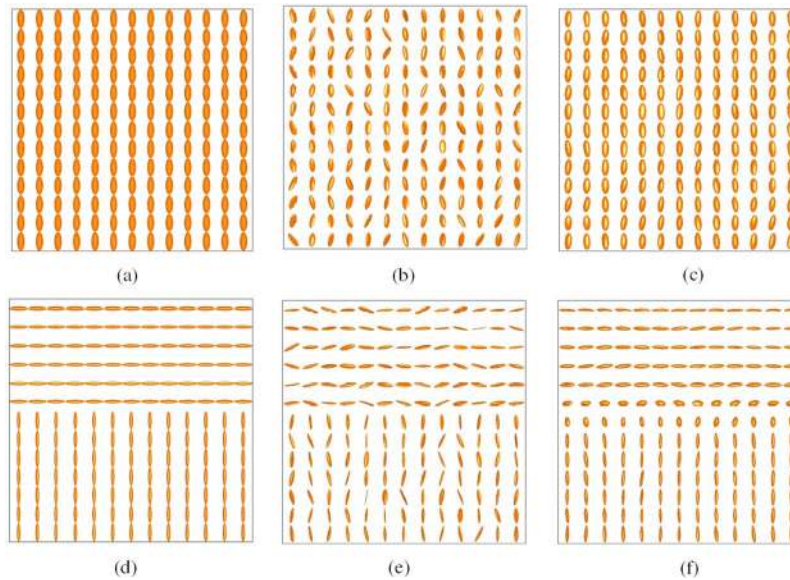
Fig. 1.   Smoothing of two synthetic tensor fields. (a) Original homogeneous tensor field. (d) Another original tensor field that contains an interface. (b), (e) Noisy version of (a) and (d), respectively, while (c) and (f) show the smoothing results on (b) and (e). $d_{T_J}, \alpha = 0.2, N = 8$ are used as an example. The effect of changing these parameters is shown in other figures.

In this section, we present qualitative and quantitative bilateral filtering based smoothing and interpolation results of synthetic diffusion tensor fields and real cardiac and brain DTMRI data. We also demonstrate the effect of bilateral filtering on diffusion tensor image segmentation.

### A.  Results on Synthetic Data

For validating our method (Sections III-A2 and III-A3), we made use of two synthetic data sets. The first data set contains a homogeneous DT field whereas the other contains a clear interface between two regions with different diffusion properties [Fig. 1(a) and (d)]. Noisy DTMRI images were produced by adding random Gaussian noise independently to the three eigen values (as in [4]), in addition to random rotation (in azimuth and elevation) perturbing the three eigen vectors by the same amount to retain orthogonality [Fig. 1(b) and (e)]. Example bilateral smoothing results on the two data sets are shown for illustration [Fig. 1(c) and (f)].

*1) Comparing Bilateral Filtering and Simple Averaging:* In Fig. 2, we demonstrate the edge preserving quality of the proposed bilateral filtering by comparing it to spatial Log-Euclidean averaging that does not take tensor distance into account. The figure shows that spatial-only averaging blurs the interface between the two regions of different anisotropic diffusion properties, resulting in more isotropic tensors near the interface [Fig. 2(a)] compared to bilateral filtering [Fig. 2(b)].

To quantitatively examine the effect of smoothing on blurring the interface between the regions of different diffusion properties, we evaluated two measures of diffusion anisotropy (FA and RA) of tensor pixels along the interface. Since at either side of the interface the diffusion was highly anisotropic [but in different directions as shown in Fig. 1(d)], retaining high anisotropy of the interface pixels means that less undesirable blurring at the interface is achieved. Table I shows that when using the proposed bilateral DT smoothing, higher FA and RA
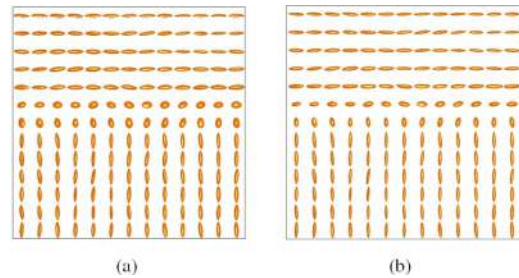


Fig. 2.   Comparison between equal-weight averaging and bilateral filtering results. The interface data set of Fig. 1 is filtered using (a) Log-Euclidean averaging and (b) the proposed method ($N = 9, \alpha = 1, d_{T_J}$) after one iteration. Note how the tensors at the interface become more isotropic in (a) compared to (b). This is also demonstrated by averaging the RA and FA values for the tensors in the two middle rows (Table I).

TABLE I
COMPARISON OF DIFFUSION ANISOTROPY MEASURES AT THE INTERFACE
PIXELS AFTER ALTERNATIVE SMOOTHING APPROACHES

| Measure | Original Data | Equal-weight Log-Euclidean Averaging | Bilateral Filtering (spatial distance) | Bilateral Filtering (spatial and tensor distance) |
|---------|---------------|--------------------------------------|----------------------------------------|---------------------------------------------------|
| FA | 0.789 | 0.3971 | 0.4508 | 0.5359 |
| RA | 0.5979 | 0.2426 | 0.2803 | 0.3448 |

are obtained (more anisotropic, i.e., less interface blurring) compared to simple equal-weight Log-Euclidean averaging of tensors. The reported FA and RA values are the average values of the interface pixels (the two middle rows of Fig. 2).

In Fig. 3, we compare the error values when smoothing the interface data using equal-weight Log-Euclidean averaging (that does not take spatial distance nor tensor distance into account), bilateral filtering with $\alpha = 0$ (taking only spatial distance into account when calculating the weights), bilateral filtering with

Fig. 3. Comparison between different alternative DT smoothing methods. The tensor field with an interface [Fig. 1(d)] is used. In (a), "None" denotes that no smoothing is performed. "Ave." denotes equal-weight 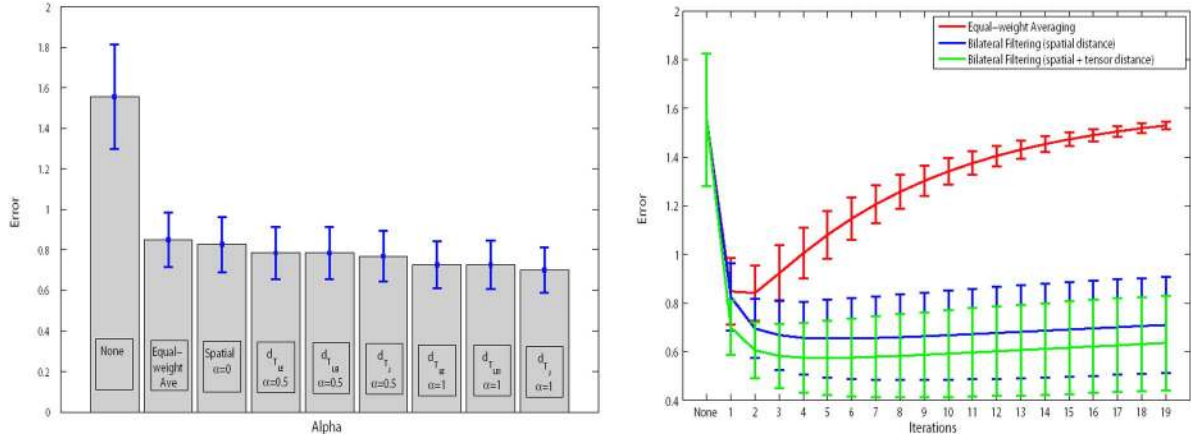Log-Euclidean averaging. "Spatial" denotes bilateral filtering with $\alpha = 0$ (considering only spatial distance but not tensor distance). For bars with $\alpha \neq 0$, the value of $\alpha$ and the tensor dissimilarity measure are indicated (including the cases when $\alpha = 1$, where only tensor distance is considered). The vertical axis indicates error values (as explained in the text at the end of Section III-A1). (b) Red: Equal-weight averaging without considering tensor or spatial distance. Blue: Weighted averaging according to spatial distance only ($\alpha = 0$). Green: Bilateral filtering taking both spatial distance and tensor distance into account ($\alpha = 0.5, d_{T_J}$). For all cases, $N = 9$. The error in all cases is calculated using $d_{T_{LE}}$. The figure clearly shows that bilateral filtering outperforms simple averaging. As the number of iterations increases, simple averaging blurs the interface significantly compared to bilateral filtering. Note also how considering both spatial and tensor distances improves the results compared to utilizing only the spatial distance.
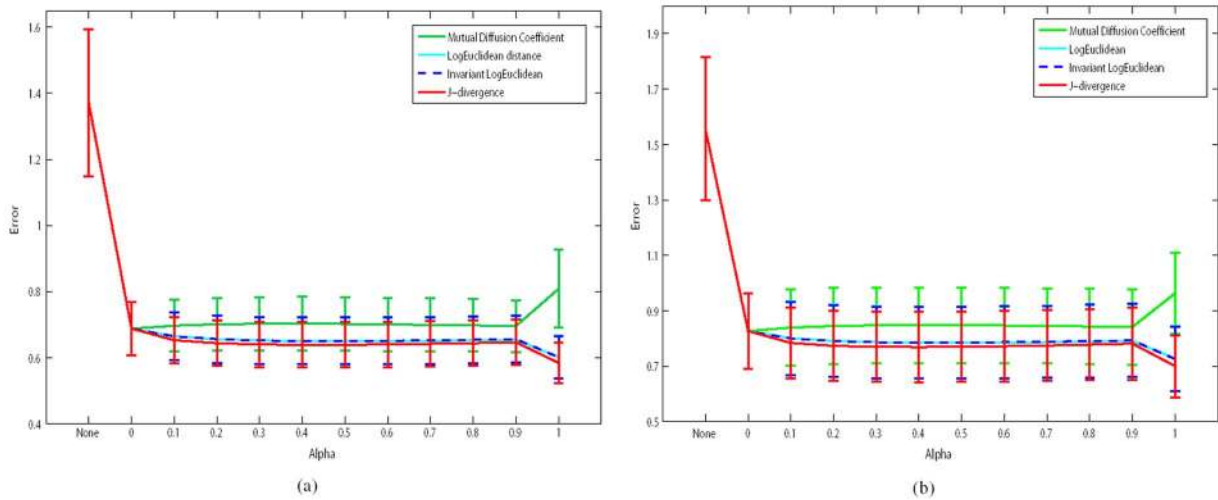


Fig. 4. Effect of $\alpha$ on denoising synthetic data. Mean error values shown are calculated by averaging all the tensor distances between corresponding pixels in the denoised image and the original image. Mean and standard deviation of error are shown for different values of $\alpha$. The first error entry (at "None") represents the error of the noisy image. The error results are measured using $d_{T_J}$ for (a) the homogeneous tensor field [Figs. 1(b)] and for (b) the DT field with the interface [Fig. 1(e)]. Note the decrease in error for a wide range of $\alpha$ (the error increased for $\alpha = 1$ when using $d_{T_k}$). Figs. 5 and 6 may be useful to relate these distances to tensors differences.

$\alpha = 1$ (considering only tensor distance), and bilateral filtering with other $\alpha$ values (considering both spatial and tensor distance when calculating the weights). The figure shows improved performance (lower error values) of bilateral filtering over simple equal-weight averaging.

In Fig. 3 and in subsequent quantitative experiments and validation results, the error calculations are obtained by creating 15 noisy images, smoothing them with different values of $\alpha$ or over several iterations, and estimating the mean error and standard derivation of the difference between the smoothed DT field to the (known) noise-free original. The different tensor distance measures ($d_{T_{LE}}$, $d_{T_{LEI}}$, $d_{T_J}$, and $d_{T_K}$) and linear and logarithmic mapping functions $f_1$ and $f_2$ were evaluated. Almost identical results are obtained when using different tensor distance measures for error calculations. The mapping functions had little impact on the results. The error difference is calculated by averaging all the tensor distances between corresponding pixels in the denoised image and the original image.

*2) Effect of Alpha on Bilateral DT-Smoothing:* As mentioned earlier $\alpha$ controls the relative emphasis on spatial versus tensor distance. The noisy images are smoothed using $\alpha$ ranging from 0.0 to 1.0 in increments of 0.1 (Fig. 4). The overall observation is a decrease in the error for $0.1 < \alpha < 0.9$, compared to the error of the noisy tensor field. The error was less even for $\alpha = 1$ for all distance measures except for $d_{T_k}$, given its dependence on the choice of $x_1$ and $x_2$. Similar behavior was obtained over several noise levels (clearly, with higher error values for stronger noise).

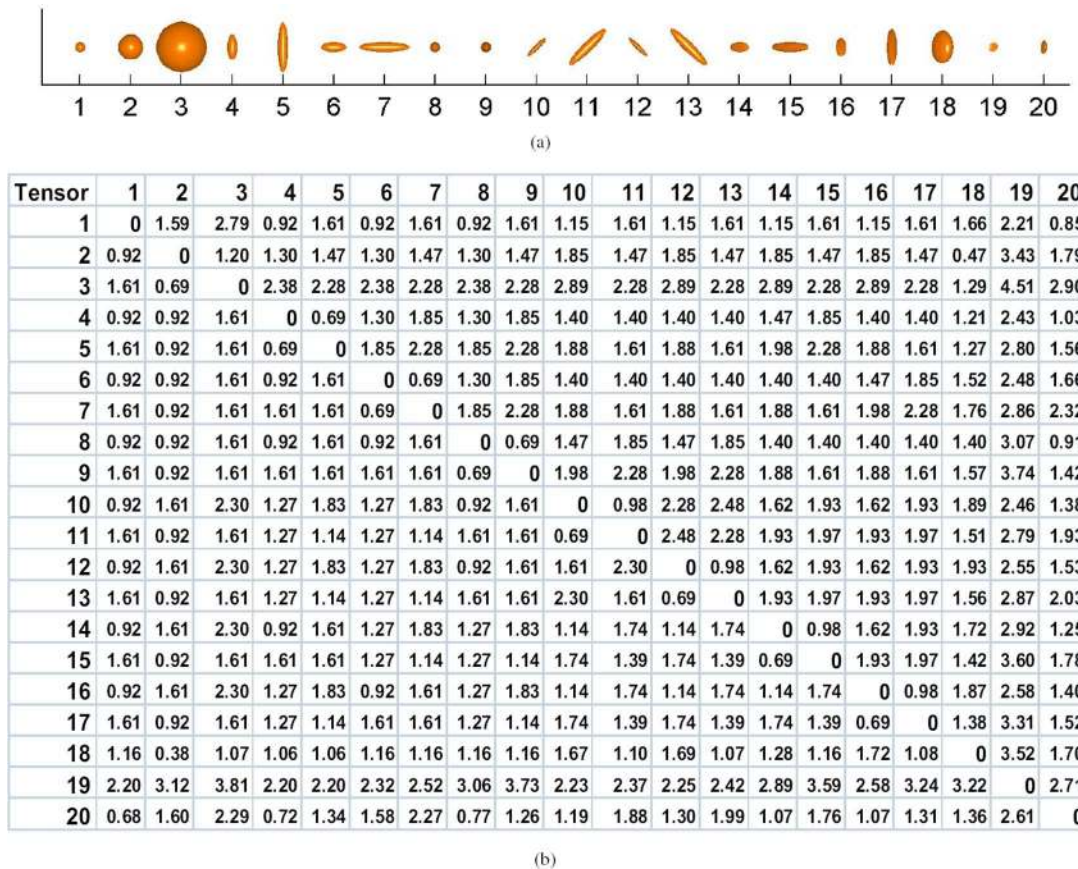| Tensor | 1 | 2 | 3 | 4 | 5 | 6 | 7 | 8 | 9 | 10 | 11 | 12 | 13 | 14 | 15 | 16 | 17 | 18 | 19 | 20 |
|---|---|---|---|---|---|---|---|---|---|---|---|---|---|---|---|---|---|---|---|---|
| 1 | 0 | 1.59 | 2.79 | 0.92 | 1.61 | 0.92 | 1.61 | 0.92 | 1.61 | 1.15 | 1.61 | 1.15 | 1.61 | 1.15 | 1.61 | 1.15 | 1.61 | 1.66 | 2.21 | 0.85 |
| 2 | 0.92 | 0 | 1.20 | 1.30 | 1.47 | 1.30 | 1.47 | 1.30 | 1.47 | 1.85 | 1.47 | 1.85 | 1.47 | 1.85 | 1.47 | 1.85 | 1.47 | 0.47 | 3.43 | 1.79 |
| 3 | 1.61 | 0.69 | 0 | 2.38 | 2.28 | 2.38 | 2.28 | 2.38 | 2.28 | 2.89 | 2.28 | 2.89 | 2.28 | 2.89 | 2.28 | 2.89 | 2.28 | 1.29 | 4.51 | 2.90 |
| 4 | 0.92 | 0.92 | 1.61 | 0 | 0.69 | 1.30 | 1.85 | 1.30 | 1.85 | 1.40 | 1.40 | 1.40 | 1.40 | 1.47 | 1.85 | 1.40 | 1.40 | 1.21 | 2.43 | 1.03 |
| 5 | 1.61 | 0.92 | 1.61 | 0.69 | 0 | 1.85 | 2.28 | 1.85 | 2.28 | 1.88 | 1.61 | 1.88 | 1.61 | 1.98 | 2.28 | 1.88 | 1.61 | 1.27 | 2.80 | 1.56 |
| 6 | 0.92 | 0.92 | 1.61 | 0.92 | 1.61 | 0 | 0.69 | 1.30 | 1.85 | 1.40 | 1.40 | 1.40 | 1.40 | 1.40 | 1.40 | 1.47 | 1.85 | 1.52 | 2.48 | 1.66 |
| 7 | 1.61 | 0.92 | 1.61 | 1.61 | 1.61 | 0.69 | 0 | 1.85 | 2.28 | 1.88 | 1.61 | 1.88 | 1.61 | 1.88 | 1.61 | 1.98 | 2.28 | 1.76 | 2.86 | 2.32 |
| 8 | 0.92 | 0.92 | 1.61 | 0.92 | 1.61 | 0.92 | 1.61 | 0 | 0.69 | 1.47 | 1.85 | 1.47 | 1.85 | 1.40 | 1.40 | 1.40 | 1.40 | 1.40 | 3.07 | 0.91 |
| 9 | 1.61 | 0.92 | 1.61 | 1.61 | 1.61 | 1.61 | 1.61 | 0.69 | 0 | 1.98 | 2.28 | 1.98 | 2.28 | 1.88 | 1.61 | 1.88 | 1.61 | 1.57 | 3.74 | 1.42 |
| 10 | 0.92 | 1.61 | 2.30 | 1.27 | 1.83 | 1.27 | 1.83 | 0.92 | 1.61 | 0 | 0.98 | 2.28 | 2.48 | 1.62 | 1.93 | 1.62 | 1.93 | 1.89 | 2.46 | 1.38 |
| 11 | 1.61 | 0.92 | 1.61 | 1.27 | 1.14 | 1.27 | 1.14 | 1.61 | 1.61 | 0.69 | 0 | 2.48 | 2.28 | 1.93 | 1.97 | 1.93 | 1.97 | 1.51 | 2.79 | 1.93 |
| 12 | 0.92 | 1.61 | 2.30 | 1.27 | 1.83 | 1.27 | 1.83 | 0.92 | 1.61 | 1.61 | 2.30 | 0 | 0.98 | 1.62 | 1.93 | 1.62 | 1.93 | 1.93 | 2.55 | 1.53 |
| 13 | 1.61 | 0.92 | 1.61 | 1.27 | 1.14 | 1.27 | 1.14 | 1.61 | 1.61 | 2.30 | 1.61 | 0.69 | 0 | 1.93 | 1.97 | 1.93 | 1.97 | 1.56 | 2.87 | 2.03 |
| 14 | 0.92 | 1.61 | 2.30 | 0.92 | 1.61 | 1.27 | 1.83 | 1.27 | 1.83 | 1.14 | 1.74 | 1.14 | 1.74 | 0 | 0.98 | 1.62 | 1.93 | 1.72 | 2.92 | 1.25 |
| 15 | 1.61 | 0.92 | 1.61 | 1.61 | 1.61 | 1.27 | 1.14 | 1.27 | 1.14 | 1.74 | 1.39 | 1.74 | 1.39 | 0.69 | 0 | 1.93 | 1.97 | 1.42 | 3.60 | 1.78 |
| 16 | 0.92 | 1.61 | 2.30 | 1.27 | 1.83 | 0.92 | 1.61 | 1.27 | 1.83 | 1.14 | 1.74 | 1.14 | 1.74 | 1.14 | 1.74 | 0 | 0.98 | 1.87 | 2.58 | 1.40 |
| 17 | 1.61 | 0.92 | 1.61 | 1.27 | 1.14 | 1.61 | 1.61 | 1.27 | 1.14 | 1.74 | 1.39 | 1.74 | 1.39 | 1.74 | 1.39 | 0.69 | 0 | 1.38 | 3.31 | 1.52 |
| 18 | 1.16 | 0.38 | 1.07 | 1.06 | 1.06 | 1.16 | 1.16 | 1.16 | 1.16 | 1.67 | 1.10 | 1.69 | 1.07 | 1.28 | 1.16 | 1.72 | 1.08 | 0 | 3.52 | 1.70 |
| 19 | 2.20 | 3.12 | 3.81 | 2.20 | 2.20 | 2.32 | 2.52 | 3.06 | 3.73 | 2.23 | 2.37 | 2.25 | 2.42 | 2.89 | 3.59 | 2.58 | 3.24 | 3.22 | 0 | 2.71 |
| 20 | 0.68 | 1.60 | 2.29 | 0.72 | 1.34 | 1.58 | 2.27 | 0.77 | 1.26 | 1.19 | 1.88 | 1.30 | 1.99 | 1.07 | 1.76 | 1.07 | 1.31 | 1.36 | 2.61 | 0 |

(b)

Fig. 5. Diffusion tensor distances. (a) Variety of DTs visualized using the common 3-D ellipsoidal glyph whose orientations are given by the eigenvectors and the length of their semi-axes by the eigenvalues of the DT. (b) $d_{T_{1,F}}$ and $d_{T_{1,FI}}$ (lower and upper triangle, respectively) distances between pairs of ellipsoids. The first three DTs (1, 2, 3) are isotropic with $\lambda = 1, 2.5, 5$. The next three pairs (4–5, 6–7, 8–9) have $\lambda_1 = 5$ or 2.5, and $\lambda_2 = \lambda_3 = 1$, and are oriented along $x$, $y$, and $z$, respectively. The next four pairs (10–11, to 16–17) are $45°$-rotated versions of tensors 4 to 9. The last three tensors are randomly selected real DTMRI tensors.

To interpret these results, it is insightful to provide an intuitive means of relating DT distance measures to differences in diffusion properties (Figs. 5 and 6).

*3) Effect of Number of Iterations on Bilateral DT-Smoothing:* For a given $\alpha$, the images were repeatedly smoothed (Fig. 7). Note the tendency of the error to decrease as the number of iterations is increased when smoothing the DT field without the interface. Also note the significant drop in error within the first few iterations for both data sets (with and without an interface; Fig. 7). For the interface data, we note a slight increase in error as more smoothing iterations are performed. This is expected and is attributed to the eventual blurring of the interface with excessive iterations.

In Fig. 7, we compare the effect of applying multiple smoothing iterations for equal-weight Log-Euclidean averaging and bilateral smoothing on the interface data set. Although both methods of filtering reduce the error in the first iteration, Fig. 7 clearly shows superior noise reduction for all iterations when using the proposed bilateral DT filtering.

### B. Comparing DT Dissimilarity Metrics

In order to evaluate the performance using different tensor dissimilarity metrics within the Log-Euclidean weighted averaging framework, and to validate that it is sensible to use dissimilarity metrics other than those based on the Log-Eu-

clidean framework ($d_{T_{1,F}}$ and $d_{T_{1,FI}}$), namely $d_{T_J}$ and $d_{T_K}$, for Log-Euclidean based weighted averaging, we performed the following experiment. For each pair of tensors ($T_i$, $T_j$) in Fig. 5, we performed Log-Euclidean weighted averaging with $w_i = 0, 0.1, \ldots, 1$ weighting $T_i$ and $1 - w_i$ weighting $T_j$ [according to (3)]. Hence, we obtain an average tensor $\bar{T}$ for each case. We then measured the distances, using the four different tensor dissimilarity metrics ($d_{T_{1,F}}, d_{T_{1,FI}}, d_{T_J}$, and $d_{T_K}$), between $T_i$ and $\bar{T}$ and between $T_j$ and $\bar{T}$. We then demonstrated, through scatter plots and correlation coefficients, that these distances to the average indeed correlate with the assigned weights, regardless of the distance metric used within the Log-Euclidean weighted averaging framework. The details of the experiment and the results are reported in Fig. 8. Fig. 8 also shows the correlation between the different DT distance metrics using the same pairs of tensors. Note that the $d_{T_K}$ is removed from the comparison since its performance requires the specification of a spatial location for each tensor, which is not relevant in this comparison.

### C. Smoothing Results on Real DTMRI Data

We applied the proposed bilateral DT smoothing algorithm on real brain [Fig. 9(a)] and cardiac [Fig. 9(b)] DTMRI data. Examples of cardiac and brain DTMRI edge-preserving smoothing results are presented in Figs. 10 and 11.
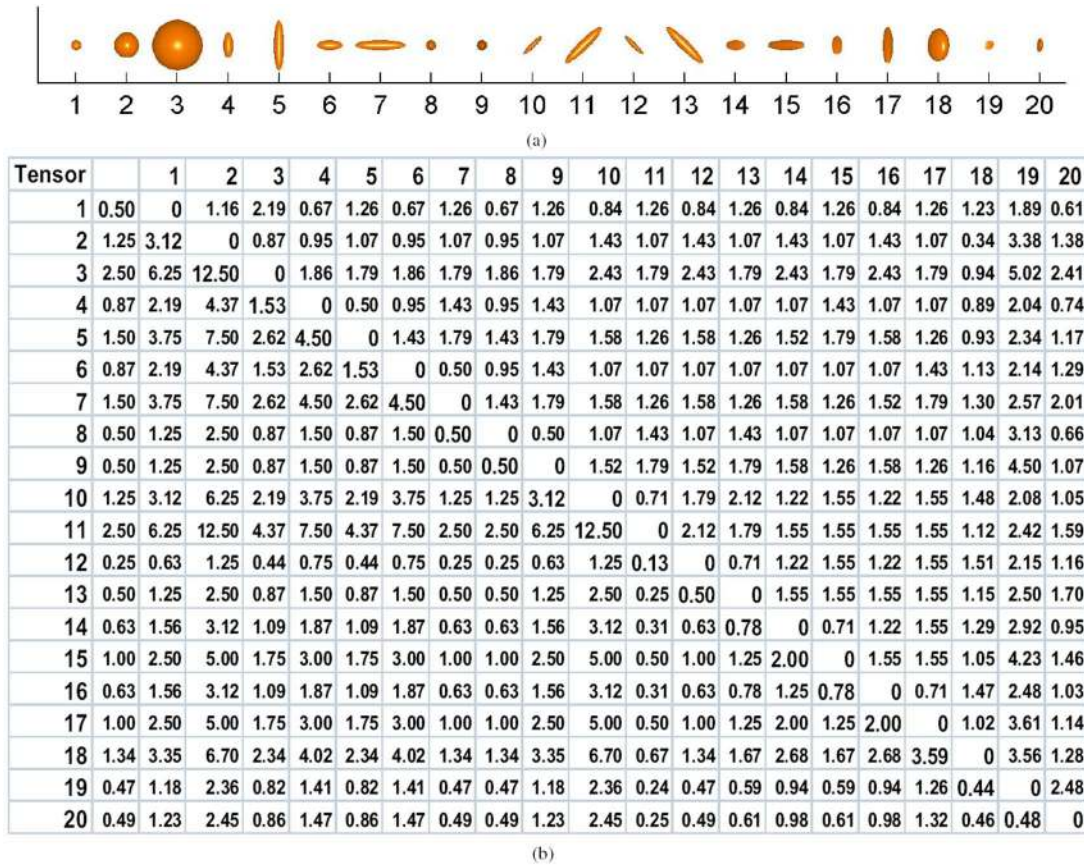
| Tensor | 1 | 2 | 3 | 4 | 5 | 6 | 7 | 8 | 9 | 10 | 11 | 12 | 13 | 14 | 15 | 16 | 17 | 18 | 19 | 20 |
|---|---|---|---|---|---|---|---|---|---|---|---|---|---|---|---|---|---|---|---|---|
| 1 | 0.50 | 0 | 1.16 | 2.19 | 0.67 | 1.26 | 0.67 | 1.26 | 0.67 | 1.26 | 0.84 | 1.26 | 0.84 | 1.26 | 0.84 | 1.26 | 0.84 | 1.26 | 1.23 | 1.89 | 0.61 |
| 2 | 1.25 | 3.12 | 0 | 0.87 | 0.95 | 1.07 | 0.95 | 1.07 | 0.95 | 1.07 | 1.43 | 1.07 | 1.43 | 1.07 | 1.43 | 1.07 | 1.43 | 1.07 | 0.34 | 3.38 | 1.38 |
| 3 | 2.50 | 6.25 | 12.50 | 0 | 1.86 | 1.79 | 1.86 | 1.79 | 1.86 | 1.79 | 2.43 | 1.79 | 2.43 | 1.79 | 2.43 | 1.79 | 2.43 | 1.79 | 0.94 | 5.02 | 2.41 |
| 4 | 0.87 | 2.19 | 4.37 | 1.53 | 0 | 0.50 | 0.95 | 1.43 | 0.95 | 1.43 | 1.07 | 1.07 | 1.07 | 1.07 | 1.07 | 1.43 | 1.07 | 1.07 | 0.89 | 2.04 | 0.74 |
| 5 | 1.50 | 3.75 | 7.50 | 2.62 | 4.50 | 0 | 1.43 | 1.79 | 1.43 | 1.79 | 1.58 | 1.26 | 1.58 | 1.26 | 1.52 | 1.79 | 1.58 | 1.26 | 0.93 | 2.34 | 1.17 |
| 6 | 0.87 | 2.19 | 4.37 | 1.53 | 2.62 | 1.53 | 0 | 0.50 | 0.95 | 1.43 | 1.07 | 1.07 | 1.07 | 1.07 | 1.07 | 1.07 | 1.07 | 1.43 | 1.13 | 2.14 | 1.29 |
| 7 | 1.50 | 3.75 | 7.50 | 2.62 | 4.50 | 2.62 | 4.50 | 0 | 1.43 | 1.79 | 1.58 | 1.26 | 1.58 | 1.26 | 1.58 | 1.26 | 1.52 | 1.79 | 1.30 | 2.57 | 2.01 |
| 8 | 0.50 | 1.25 | 2.50 | 0.87 | 1.50 | 0.87 | 1.50 | 0.50 | 0 | 0.50 | 1.07 | 1.43 | 1.07 | 1.43 | 1.07 | 1.07 | 1.07 | 1.07 | 1.04 | 3.13 | 0.66 |
| 9 | 0.50 | 1.25 | 2.50 | 0.87 | 1.50 | 0.87 | 1.50 | 0.50 | 0.50 | 0 | 1.52 | 1.79 | 1.52 | 1.79 | 1.58 | 1.26 | 1.58 | 1.26 | 1.16 | 4.50 | 1.07 |
| 10 | 1.25 | 3.12 | 6.25 | 2.19 | 3.75 | 2.19 | 3.75 | 1.25 | 1.25 | 3.12 | 0 | 0.71 | 1.79 | 2.12 | 1.22 | 1.55 | 1.22 | 1.55 | 1.48 | 2.08 | 1.05 |
| 11 | 2.50 | 6.25 | 12.50 | 4.37 | 7.50 | 4.37 | 7.50 | 2.50 | 2.50 | 6.25 | 12.50 | 0 | 2.12 | 1.79 | 1.55 | 1.55 | 1.55 | 1.55 | 1.12 | 2.42 | 1.59 |
| 12 | 0.25 | 0.63 | 1.25 | 0.44 | 0.75 | 0.44 | 0.75 | 0.25 | 0.25 | 0.63 | 1.25 | 0.13 | 0 | 0.71 | 1.22 | 1.55 | 1.22 | 1.55 | 1.51 | 2.15 | 1.16 |
| 13 | 0.50 | 1.25 | 2.50 | 0.87 | 1.50 | 0.87 | 1.50 | 0.50 | 0.50 | 1.25 | 2.50 | 0.25 | 0.50 | 0 | 1.55 | 1.55 | 1.55 | 1.55 | 1.15 | 2.50 | 1.70 |
| 14 | 0.63 | 1.56 | 3.12 | 1.09 | 1.87 | 1.09 | 1.87 | 0.63 | 0.63 | 1.56 | 3.12 | 0.31 | 0.63 | 0.78 | 0 | 0.71 | 1.22 | 1.55 | 1.29 | 2.92 | 0.95 |
| 15 | 1.00 | 2.50 | 5.00 | 1.75 | 3.00 | 1.75 | 3.00 | 1.00 | 1.00 | 2.50 | 5.00 | 0.50 | 1.00 | 1.25 | 2.00 | 0 | 1.55 | 1.55 | 1.05 | 4.23 | 1.46 |
| 16 | 0.63 | 1.56 | 3.12 | 1.09 | 1.87 | 1.09 | 1.87 | 0.63 | 0.63 | 1.56 | 3.12 | 0.31 | 0.63 | 0.78 | 1.25 | 0.78 | 0 | 0.71 | 1.47 | 2.48 | 1.03 |
| 17 | 1.00 | 2.50 | 5.00 | 1.75 | 3.00 | 1.75 | 3.00 | 1.00 | 1.00 | 2.50 | 5.00 | 0.50 | 1.00 | 1.25 | 2.00 | 1.25 | 2.00 | 0 | 1.02 | 3.61 | 1.14 |
| 18 | 1.34 | 3.35 | 6.70 | 2.34 | 4.02 | 2.34 | 4.02 | 1.34 | 1.34 | 3.35 | 6.70 | 0.67 | 1.34 | 1.67 | 2.68 | 1.67 | 2.68 | 3.59 | 0 | 3.56 | 1.28 |
| 19 | 0.47 | 1.18 | 2.36 | 0.82 | 1.41 | 0.82 | 1.41 | 0.47 | 0.47 | 1.18 | 2.36 | 0.24 | 0.47 | 0.59 | 0.94 | 0.59 | 0.94 | 1.26 | 0.44 | 0 | 2.48 |
| 20 | 0.49 | 1.23 | 2.45 | 0.86 | 1.47 | 0.86 | 1.47 | 0.49 | 0.49 | 1.23 | 2.45 | 0.25 | 0.49 | 0.61 | 0.98 | 0.61 | 0.98 | 1.32 | 0.46 | 0.48 | 0 |

(b)

Fig. 6. Diffusion tensor distances. (a) Same as in Fig. 5. (b) $d_{T_J}$ and $d_{T_K}$ (lower and upper triangle, respectively) distances between pairs of ellipsoids. For $d_{T_K}$, the coordinates $x_1 = (0,0,0)$ and $x_2 = (1,1,0)$ are used [see (9)].
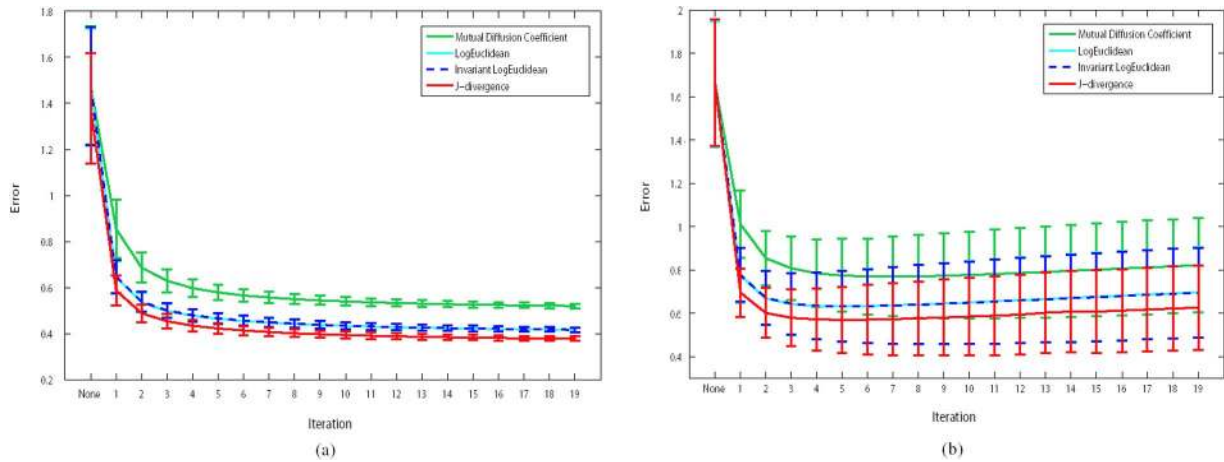


Fig. 7. Effect of number of iterations on bilateral DT smoothing. This figure depicts the error values as the number of bilateral filtering iterations is increased, from 1 to 19 iterations. Iteration 0 (at "None") corresponds to the noisy image without filtering. The error is calculated as the average tensor distance between the smoother and the original image. Note the sharp decrease in error in the first few iterations. In (a), the original image did not contain any clear boundaries, whereas (b) contained a clear edge [similar to Fig. 1(e)]. We attribute the gradual increase in error after iteration 5 in (b) to the eventual blurring of the interface if excessive smoothing iterations are performed. The error is measured using $d_{T_J}$, $\alpha = 1$, and $N = 8$.

## D. Interpolation

Interpolation of cardiac and brain DTMRI data is presented in Fig. 12. To quantitatively assess the interpolation, we compared the original data with the result of interpolation using a subsampled version of the original data. The error, calculated as the average tensor distance, $d_{T_J}$, over all voxels, was about 0.7 when every second DT was used to interpolate, compared to 1.41 with every sixth voxel. The corresponding values for $d_{T_{I,F}}$ were 0.8 and 1.34.

## E. Effect of Bilateral Filtering on Livewire Segmentation

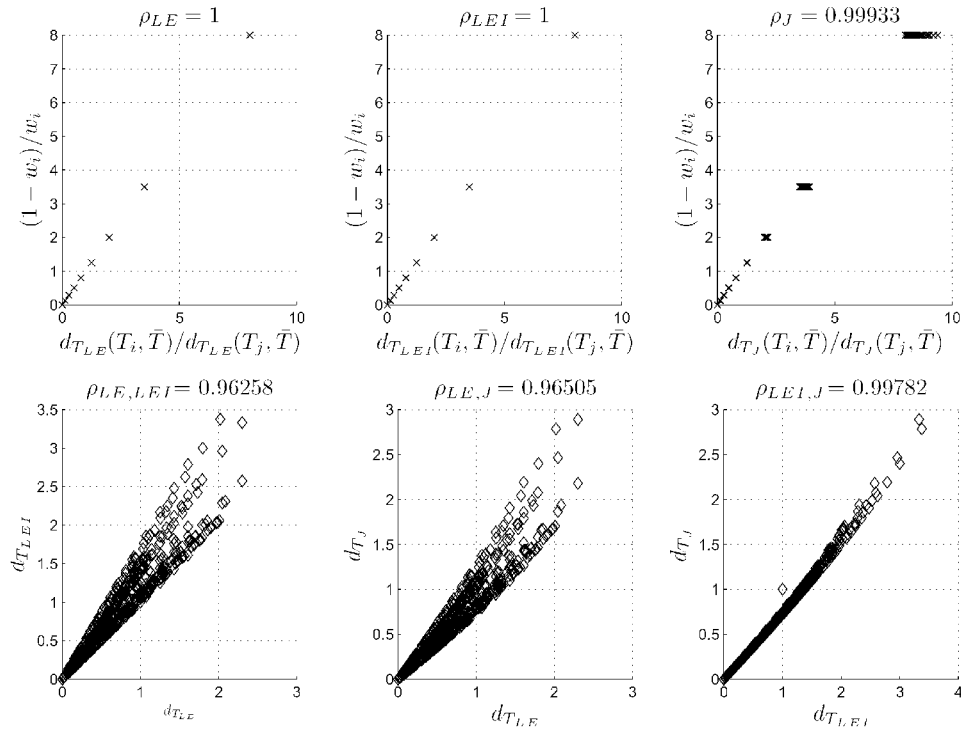We show examples of how bilateral DT filtering improves segmentation. Segmentation improvement after bilateral DT

Fig. 8. Comparing DT dissimilarity metrics. See text for details. (Top row) Given any pair of tensors $(T_i, T_j)$ from Fig. 5, the Log-Euclidean weighted average, $\bar{T}$, is calculated for each $w_i = 0, 0.1, \ldots, 1$ and $1 - w_i$. Scatter plots and correlation coefficients, $\rho$, between the two ratios are presented. The first ratio, $(1 - w_i)/w_i$, reflects the desired weighting between $T_i$ and $T_j$. The second ratio, $d_T(T_i, \bar{T})/d_T(T_j, \bar{T})$, reflects the relative distances from each of the two tensors to the calculated mean. Ideally, perfect correlation should be observed between these two ratios, $\rho = 1$. The three top figures show the scatter plots and the calculated $\rho$ when using each of the tensor dissimilarity metrics $d_{T_{LE}}$, $d_{T_{LEI}}$, and $d_{T_J}$ (denoted with subscripts LE, LEI, and J, respectively). (Bottom row) Scatter plots and correlation coefficients between the different tensor metrics for the same pairs of tensors.
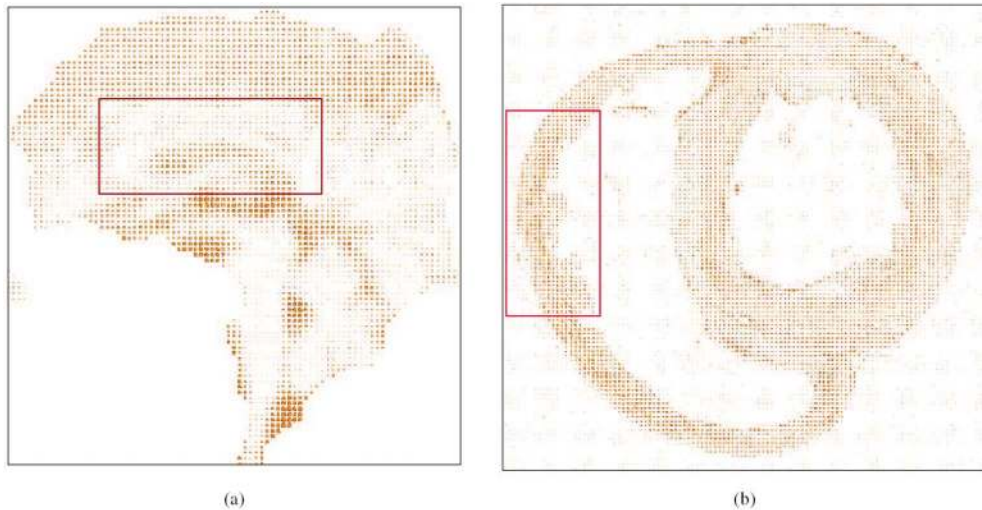


Fig. 9. Real DTMRI (a) mid-sagittal brain slice and (b) axial heart slice. The two region highlighted with the smaller rectangles are used in subsequent figures and examples.

filtering is manifested in two ways: a) less user interaction produces results of comparable quality; or b) improved segmentation quality is attained with the same amount of user interaction. In particular, user interaction is quantified by counting the number of livewire seed points. Towards this goal, we used DT-Livewire [47]; an extension of livewire for scalar and color images to DTMRI [48], [49]. The livewire defines local cost between neighboring pixels in order to calculate globally optimal paths. These paths delineate boundaries of

target structures between interactively-selected seed and target points in the image. In addition to internal cost terms that encode path smoothness, external cost terms are encoded, which favor paths (delineation) along boundaries with high gradient magnitude, while minimizing change in gradient direction. While internal terms need not be extended to deal with DTMRI data, external terms do because they depend on image data. Consequently, *diffusion tensor gradient vector*, $\nabla T$ at any location $(x, y)$, is defined by replacing the scalar finite difference
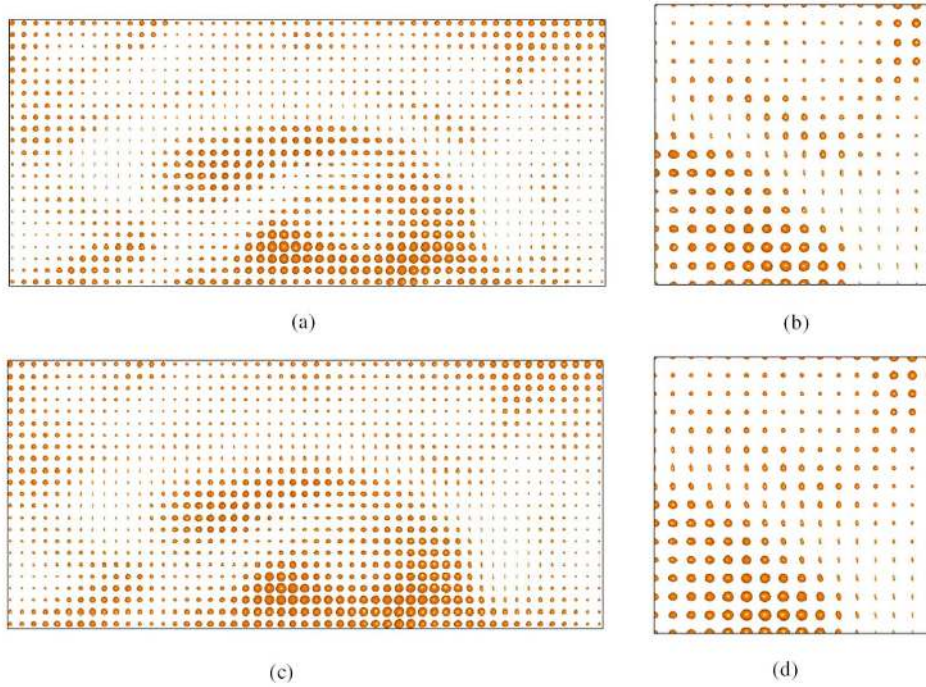
Fig. 10. Bilateral smoothing of the corpus callosum in brain DTMRI. Original and smoothed corpus callosum shown in (a) and (c), respectively. (b), (d) Scaled up regions of the original and smoothed data, respectively.
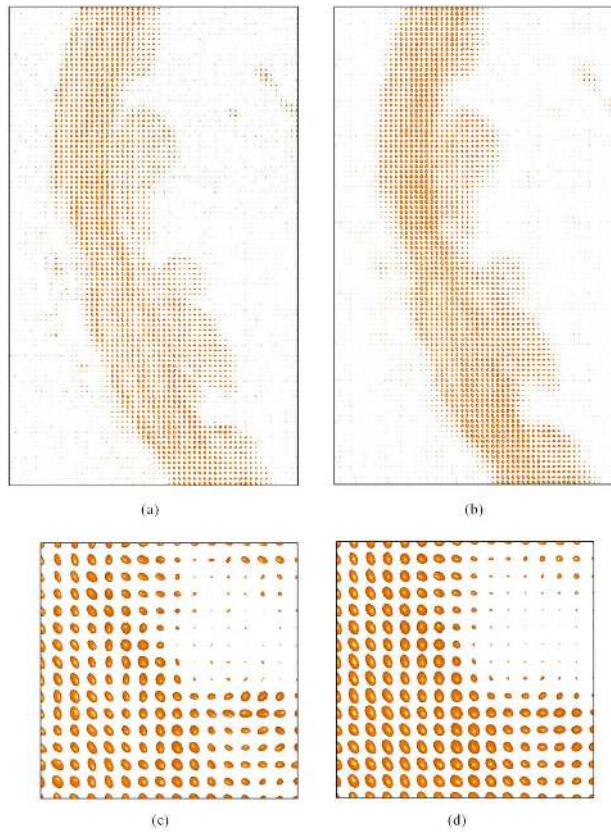


Fig. 11. Bilateral smoothing of the myocardium in cardiac DTMRI. Original and smoothed heart wall shown in (a) and (b), respectively. (c), (d) Scaled up regions of the original and smoothed data, respectively.

(subtraction) approximation with central tensor dissimilarity metrics, as follows:

$$\nabla T(x,y) = \frac{1}{2} \begin{bmatrix} d_T(T(x+1,y), T(x-1,y)) \\ d_T(T(x,y+1), T(x,y-1)) \end{bmatrix} \quad (10)$$

where $\nabla$ now operates on a diffusion tensor field and $d_T$ is one of the tensor distance measures presented earlier [(6)–(9)]. In DT-Livewire, the full information in the tensors is utilized, without being forced to operate on a single derived scalar image such as ADC or RA [3]. The reader is referred to [48] for details
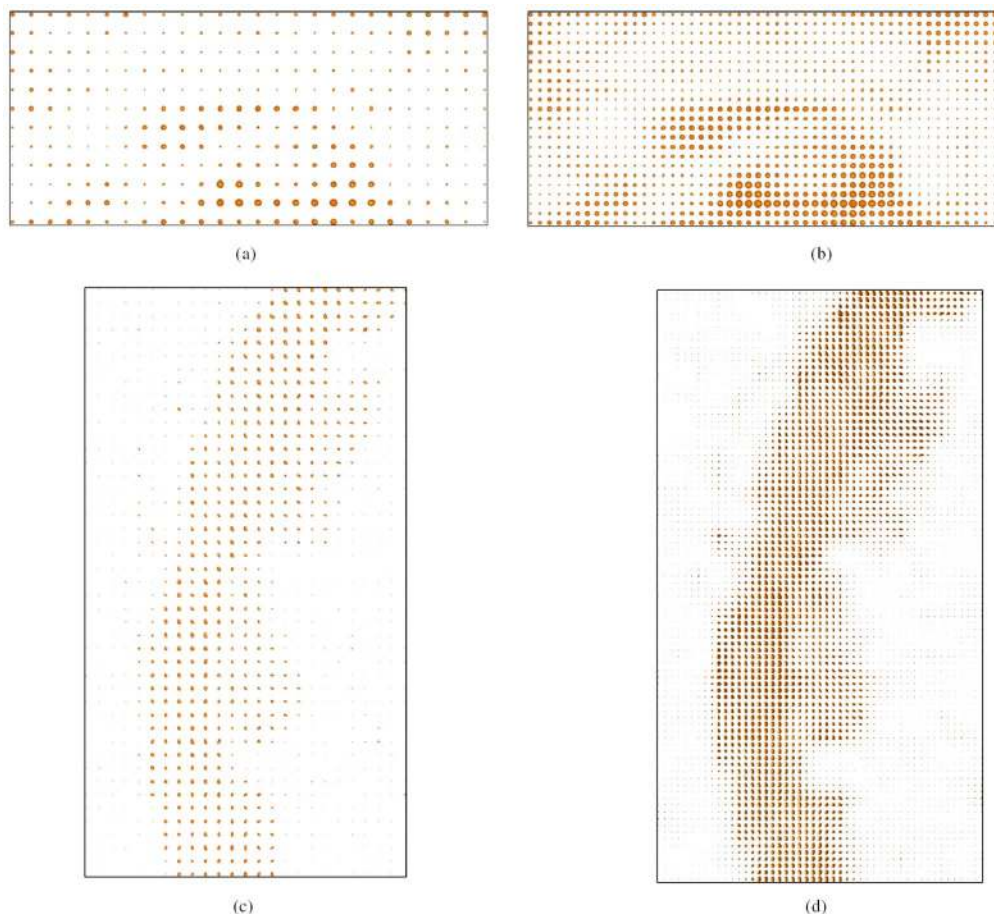
Fig. 12.   Interpolation examples of real brain and cardiac DTMRI data. (a), (c) Coarse brain and heart data; (b), (d) corresponding interpolation results.
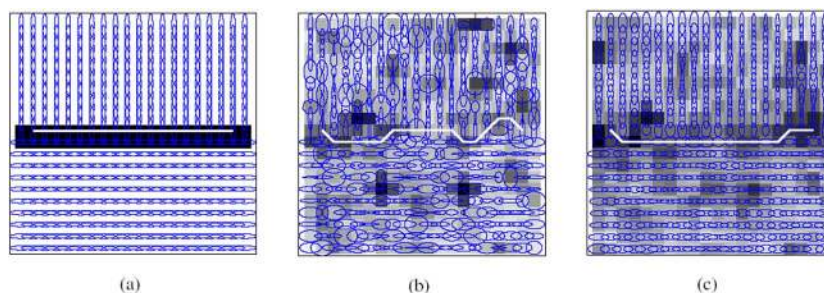


Fig. 13.   Effect of smoothing on DT-Livewire segmentation. In (a)–(c), a DT-Livewire is supplied with the same seed points (terminal points of the white livewire contour). In (a), the DT-Livewire is operating on a noise-free synthetic DT field exhibiting two homogeneous regions (top and bottom halves) with different diffusion properties. The livewire successfully latches along the DT interface. In (b), DT-Livewire is operating on a noisy version of (a) and the livewire contour deviates from the correct interface. In (c), the DT field is smoothed using the proposed bilateral filtering (with $d_{T_J}$, $\alpha = 0.2$, N $= 9$, and 1 iteration), and an improved DT-Livewire delineation result is obtained. The diffusion tensors are displayed as blue ellipses with eccentricity reflecting the ratio between the two largest eigenvalues.

on the derivations of the scalar versions of external cost terms, noting that instead of scalar gradients, tensor gradients are used as in (10).

In Fig. 13, we demonstrate the effect of Bilateral DT filtering on the performance of DT-Livewire segmentation, given the same number and same location of seed points, while changing the amount of noise in the DT image. DT-Livewire performs as expected when no noise is introduced and manages to identify the interface between two homogeneous regions with different diffusion properties. The performance deteriorates when noise

is added to the image and improves again when applying bilateral DT filtering to reduce the noise.

In Fig. 14, we apply DT-Livewire to the segmentation of the endocardium from heart DTMRI. This example demonstrates that livewire now operates on tensor data, as evidenced by the livewire contour latching to inner heart wall between successive seed points. This example also demonstrates bilateral smoothing of DT fields and how it reduces the amount of seed points required to complete the livewire segmentation, compared to the original noisy data.
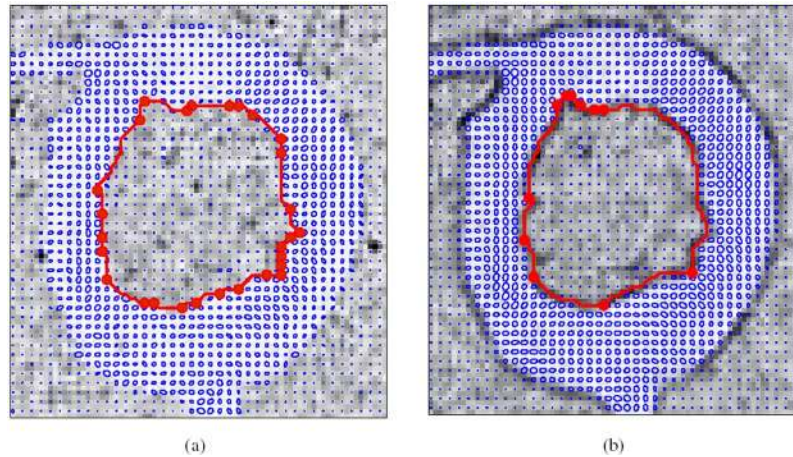
Fig. 14.　Segmentation of the endocardium from heart DTMRI using DT-Livewire. DT-Livewire is applied to (a) the original noisy DTMRI slice and to (b) a smoothed version of the DT data (Section II). Less number of user-selected seed points are required for segmentation when the data is smoothed. The DT-Livewire contour is shown in red and seed points are shown as solid red circles. Diffusion tensors and backdrop are visualized as in earlier figures.
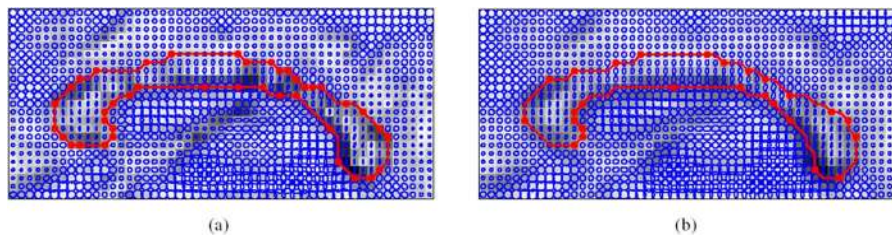


Fig. 15.　Segmentation of the corpus callosum from brain DTMRI using DT-Livewire. DT-Livewire is applied to (a) the original noisy DTMRI slice and to (b) a smoothed version of the DT data. Less number of user-selected seed points are required for perform segmentation when the data is smoothed (smoothing and legend are as described in Fig. 14).

In Fig. 15, we segment the corpus callosum from brain DTMRI using DT-Livewire. As in the previous example, smoothing results are visualized and its effect on DT-Livewire segmentation is demonstrated, namely reducing the number of seed points the user needs to manually specify.

## IV. Conclusion

DTMRI provides unique *in vivo* measurements of fibre structure in the body. The measurements are presented as 2-D or 3-D images where each pixel or voxel holds a $3 \times 3$ matrix. There is a strong interest in the biomedical image computing community to process, visualize, and analyze this type of data in order to extract clinically relevant information related to diagnosis and therapy of cardiac, neurological, and other pathologies. However, the majority of existing techniques are designed to operate on scalar fields (or RGB color images) and more work is needed to provide a diverse set of algorithms and tools at par with what is available for scalar images.

In this paper, we extended bilateral image filtering to diffusion tensor field data. Making use of the Log-Euclidean framework and tensor dissimilarity metrics. We defined diffusion tensor interpolation as a special case of bilateral tensor field filtering. Quantitative and qualitative results showed that the DT bilateral filtering is successful in preserving diffusion tensor interfaces. The results also showed that the performance of square root of the J-divergence distance is comparable to the Log-Euclidean distances, and that the distance scaled mutual diffusion coefficient can only be used in cases where the spatial

locations of tensors are known, which limits its applicability. We also showed several examples demonstrating how bilateral DT smoothing reduced the number of manual seeding required when performing Livewire segmentation.

Future work includes extending other classical scalar image processing and analysis algorithms to operate on 3-D DT fields, the segmentation of multiple DT images related to specific clinical applications (e.g., multiple sclerosis) and examining relationships between fiber properties in segmented regions and disease progression or treatment evaluation.

## References

[1] E. O. Stejskal and J. E. Tanner, "Spin diffusion measurements: Spin echoes in the presence of a time-dependent field gradient," *J. Chem. Phys.*, vol. 42, pp. 288–292, 1965.
[2] P. Basser, J. Mattiello, and D. LeBihan, "Estimation of the effective self-diffusion tensor from the NMR spin echo," *J. Magn. Res. B*, vol. 103, no. 3, pp. 247–54, 1994.

[3]From http://www.ccbm.jhu.edu/research/DTMRIDS.php

[3] C.-F. Westin, S. E. Maier, H. Mamata, A. Nabavi, F. A. Jolesz, and R. Kikinis, "Processing and visualization of diffusion tensor MRI," *Med. Imag. Anal.*, vol. 6, no. 2, pp. 93–108, 2002.

[4] M. Welk, C. Feddern, B. Burgeth, and J. Weickert, "Median filtering of tensor-valued images," in *Pattern Recognition*, ser. Lecture Notes in Computer Science, B. Michaelis and G. Krell, Eds.  Berlin, Germany: Springer, 2003, vol. 2781, pp. 17–24.

[5] B. Burgeth, M. Welk, C. Feddern, and J. Weickert, "Morphological operations on matrix-valued images," in *Computer Vision*, ser. Lecture Notes in Computer Science, T. Pajdla and J. Matas, Eds.  Berlin, Germany: Springer, 2004, vol. 3024, pp. 155–167.

[6] C. Castano-Moraga, M. A. Rodrigues-Florido, L. Alvarez, C.-F. Westin, and J. Ruiz-Alzola, "Anisotropic interpolation of DT-MRI data," in *Proc. 7th Int. Conf. Medical Image Computing and Computer-Assisted Intervention*, Rennes, Saint Malo, France, 2004, pp. 343–350.

[7] J. Weickert and T. Brox, M. Z. Nashed and O. Scherzer, Eds., "Diffusion and regularization of vector- and matrix-valued images," *Inv. Probl., Image Anal., Med. Imag.*, vol. 313, pp. 251–268, 2002.

[8] C.-F. Westin and H. Knutson, "Tensor field regularization using normalized convolution," in *Proc. EUROCAST*, Las Palmas de Gran Canaria, Spain, 2003, vol. 2809, pp. 564–572.

[9] L. O'Donnell, W. E. L. Grimson, and C.-F. Westin, "Interface detection in DTMRI," in *Proc. 7th Int. Conf. Medical Image Computing and Computer-Assisted Intervention*, Rennes, Saint Malo, France, 2004, pp. 360–367.

[10] Z. Wang and B. Vemuri, "An affine invariant tensor dissimilarity measure and its applications to tensor-valued image segmentation," in *Proc. CVPR*, 2004, vol. 1, pp. 228–233.

[11] A. Brun, H. Knutsson, H. J. Park, M. E. Shenton, and C.-F. Westin, "Clustering fiber tracts using normalized cuts," in *Proc. 7th Int. Conf. Medical Image Computing and Computer-Assisted Intervention*, 2004, pp. 368–375.

[12] C. Feddern, J. Weickert, and B. Burgeth, "Level-set methods for tensor-valued images," in *Proc. 2nd IEEE Workshop on Variational, Geometric and Level Set Methods in Computer Vision*, Nice, France, pp. 65–72.

[13] C. Lenglet, R. Deriche, and O. Faugeras, "Inferring white matter geometry from diffusion tensor MRI: Application to connectivity mapping," in *Proc. ECCV*, 2004, vol. 4, pp. 127–140.

[14] C. Lenglet, M. Rousson, and R. Deriche, "Segmentation of 3-D probability density fields by surface evolution: Application to diffusion MRI," in *Proc. MICCAI*, 2004, vol. 1, pp. 18–25.

[15] C. Lenglet, M. Rousson, R. Deriche, O. Faugeras, S. Lehericy, and K. Ugurbil, "A Riemannian approach to diffusion tensor images segmentation," in *Proc. IPMI*, 2005, pp. 591–602.

[16] M. Rousson, C. Lenglet, and R. Deriche, "Level set and region based surface propagation for diffusion tensor MRI segmentation," in *Proc. ECCV Workshops CVAMIA and MMBIA*, 2004, pp. 123–134.

[17] R. Deriche, D. Tschumperlé, and C. Lenglet, "DT-MRI estimation, regularization and fiber tractography," *Proc. ISBI*, pp. 9–12, 2004.

[18] L. Jonasson, P. Hagmann, C. Pollo, X. Bresson, C. R. Wilson, R. Meuli, and J.-P. Thiran, "Coupled, region based level sets for segmentation of the thalamus and its subnuclei in DT-MRI," ITS Tech. Rep. 2004, vol. 20.

[19] L. Jonasson, X. Bresson, P. Hagmann, C. R. Wilson, R. Meuli, and J.-P. Thiran, "White matter fiber tract segmentation in DT-MRI using geometric flows," *Med. Image Anal.*, vol. 9, pp. 223–236, 2005.

[20] M. Wiegell, D. Tuch, H. Larson, and V. Wedeen, "Automatic segmentation of thalamic nuclei from diffusion tensor magnetic resonance imaging," *NeuroImage*, vol. 19, pp. 391–402, 2003.

[21] D. Alexander, C. Pierpaoli, P. Basser, and J. Gee, "Spatial transformations of diffusion tensor magnetic resonance images," *IEEE Trans. Med. Imag.*, vol. 20, no. 11, pp. 1131–1139, Nov. 2001.

[22] J. Ruiz-Alzola, C.-F. Westin, S. K. Warfield, C. Alberola, S. E. Maier, and R. Kikinis, "Nonrigid registration of 3-D tensor medical data," *Med. Image Anal.*, vol. 6, pp. 143–161, 2002.

[23] A. Guimond, C. R. G. Guttmann, S. K. Warfield, and C.-F. Westin, "Deformable registration of DT-MRI data based on transformation invariant tensor characteristics," in *Proc. ISBI*, Washington, DC, 2002, pp. 761–764.

[24] I. F. Talos, L. O'Donnell, C.-F. Westin, S. K. Warfield, W. M. Wells, S. S. Yoo, L. Panych, A. Golby, H. Mamata, S. E. Maier, P. Ratiu, C. G. Guttmann, P. M. L. Black, F. A. Jolesz, and R. Kikinis, "Diffusion tensor and functional MRI fusion with anatomical MRI for image guided neurosurgery," in *Proc. 6th Int. Conf. Medical Image Computing and Computer-Assisted Intervention*, Montreal, Canada, 2003, pp. 407–415.

[25] S. Zhang, D. Laidlaw, and G. Kindlmann, "Diffusion tensor MRI visualization," in *The Visualization Handbook*, C. Hansen and C. Johnson, Eds.  New York: Elsevier, 2005, pp. 327–340.

[26] G. Kindlmann, "Superquadric tensor glyphs," presented at the Joint EUROGRAPHICS IEEE TCVG Symp. Visualization, 2004.

[27] S. Zhang, C. Demiralp, and D. Laidlaw, "Visualizing diffusion tensor MR images using streamtubes and streamsurfaces," *IEEE Trans. Vis. Comput. Graph.*, vol. 9, no. 4, pp. 454–462, Oct./Dec. 2003.

[28] T. McGraw, B. Vemuri, Y. Chen, M. Rao, and T. Mareci, "DT-MRI denoising and neuronal fiber tracking," *Med. Image Anal.*, vol. 8, pp. 95–111, 2004.

[29] C. Johnson, R. MacLeod, S. Parker, and D. Weinstein, "Biomedial computing and visualization software environments," *Commun. ACM*, vol. 47, no. 11, pp. 64–71, 2004.

[30] H.-J. Park, M. E. Shenton, and C.-F. Westin, "An analysis tool for quantification of diffusion tensor imaging," in *Proc. 7th Int. Conf. Medical Image Computing and Computer-Assisted Intervention*, Rennes, Saint Malo, France, 2004, pp. 1040–1041.

[31] P. Fillard and G. Gerig, *Analysis tool for diffusion tensor MRI*, ser. Lecture Notes in Computer Science.  New York: Springer-Verlag, 2003, vol. 2879, pp. 967–968.

[32] *Camino*, [Online]. Available: http://hdl.handle.net/1926/38

[33] *A quantitative DTI fiber tract analysis suite*, [Online]. Available: http://hdl.handle.net/1926/39

[34] *DTIstudio*, [Online]. Available: http://lbam.med.jhmi.edu/DTIuser/DTIuser.asp

[35] *Inria DT track*, [Online]. Available: http://www-sop.inria.fr/asclepios/personnel/Pierre.Fillard/softwares/Fi berTracking/

[36] *Inria Tensor Viewer*, [Online]. Available: http://www-sop.inria.fr/asclepios/personnel/Pierre.Fillard/softwares/Te nsorViewer/

[37] G. Hamarneh and J. Hradsky, "Bilateral filtering of diffusion tensor MR images," in *Proc. IEEE Symp. Signal Processing and Information Technology*, 2006, pp. 508–512.

[38] V. Arsigny, P. Fillard, X. Pennec, and N. Ayache, "Log-Euclidean metrics for fast and simple calculus on diffusion tensors," *Magn. Res. Med.*, vol. 56, no. 2, pp. 411–421, Aug. 2006, pMID: 16788917.

[39] R. B. E. Yoruk and B. Acar, J. Duncan and G. Gerig, Eds., "A physical modal for DT-MRI based connectivity map computation," in *Proc. MICCAI*, 2005, pp. 213–220.

[40] C. Tomasi and R. Manduchi, "Bilateral filtering for gray and color images," in *Proc. 6th Int. Conf. Computer Vision*, Jan. 4–7, 1998, pp. 839–846.

[41] C. Wilbur, C. Albert, and C. Simon, "Trilateral filtering for biomedical images," in *Proc. IEEE Int. Symp. Biomedical Imaging: From Nano to Macro*, 2004, pp. 820–823.

[42] I. Corouge, P. Fletcher, S. Joshi, S. Gouttard, and G. Gerig, "Fiber tract-oriented statistics for quantitative diffusion tensor MRI analysis," *Proc. MICCAI*, vol. 10, pp. 786–798, 2006.

[43] X. Pennec, P. Fillard, and N. Ayache, "A Riemannian framework for tensor computing," *Int. J. Comput. Vis.*, vol. 65, no. 1, pp. 41–66, Oct. 2005.

[44] P. Fletcher and S. Joshi, *Principal Geodesic Analysis on Symmetric Spaces: Statistics of Diffusion Tensors*, ser. Lecture Notes in Computer Science.  New York: Springer-Verlag, 2004, vol. 3117, pp. 87–98.

[45] S. Witelson, "Hand and sex differences in the isthmus and genu of the human corpus callosum: A postmortem morphological study," *Brain*, vol. 112, pp. 799–835, 1989.

[46] K. Hasan, R. Gupta, R. Santos, J. Wolinsky, and P. Narayana, "Fractional diffusion tensor anisotropy of the seven segments of the normal-appearing white matter of the corpus callosum in healthy adults and relapsing remitting multiple sclerosis," *J. Magn. Res. Imag.*, vol. 21, no. 6, pp. 735–743, 2005.

[47] G. Hamarneh and J. Hradsky, "DTMRI segmentation using DT-snakes and DT-livewire," in *Proc. IEEE Int. Symp. Signal Processing and Information Technology*, 2006, pp. 513–518.

[48] W. A. Barrett and E. N. Mortensen, "Interactive live-wire boundary extraction," *Med. Image Anal.*, vol. 1, no. 4, pp. 331–341, 1996.

[49] A. Chodorowski, U. Mattsson, M. Langille, and G. Hamarneh, J. M. Fitzpatrick and J. M. Reinhardt, Eds., "Color lesion boundary detection using live wire," *SPIE Med. Imag.*, vol. 5747, no. 1, pp. 1589–1596, 2005.

**Ghassan Hamarneh** received the B.S. degree from the Department of Electrical Engineering, Jordan University, in 1995, and the M.S. degree with distinction in digital communications from the Chalmers University of Technology in 1997.

Before joining the School of Computing Science, Simon Fraser University, Burnaby, BC, Canada, as an Assistant Professor in 2003, he was a Postdoctoral Fellow at the Hospital for Sick Children, Mouse Imaging Centre, and the Department of Medical Biophysics, University of Toronto, Toronto, ON, Canada (2001-2003). He completed his doctoral studies (2001) at the Department of Signals and Systems, Chalmers University of Technology, and as a Predoctoral Research Fellow (2000-2001) at the Department of Computer Science, University of Toronto. He is the Co-Founder (2003) and Co-Director of the Medical Image Analysis Laboratory (MIAL), Simon Fraser University. His main research interests are medical image processing, segmentation and registration, and anatomical shape modelling and analysis.

**Judith Hradsky,** received the B.S. and Diplom degree in computational visualistics from the Otto-von-Guericke University, Magdeburg, Germany, in 2004 and 2005, respectively.

From 2005 to 2006, she was a Visiting Researcher for the Medical Image Analysis Lab, School of Computing Science, Simon Fraser University, Burnaby, BC, Canada. Since 2006, she has been a Research Programmer for the Multiple Sclerosis/MRI Research Group, University of British Columbia.